The Astrophysical Journal, 931:31 (10pp), 2022 May 20 https://doi.org/10.3847/1538-4357/ac63b7

Coevolution of Brightest Cluster Galaxies and Their Host Clusters in IllustrisTNG

Jubee Sohn[1], Margaret J. Geller[1], Mark Vogelsberger[2], and Ivana Damjanov[3,4]
[1] Smithsonian Astrophysical Observatory, 60 Garden Street, Cambridge, MA 02138, USA; jubee.sohn@cfa.harvard.edu
[2] Department of Physics, Kavli Institute for Astrophysics and Space Research, Massachusetts Institute of Technology, Cambridge, MA 02139, USA
[3] Department of Astronomy and Physics, Saint Mary's University, 923 Robie Street, Halifax, NS B3H 3C3, Canada
Received 2022 January 21; revised 2022 March 31; accepted 2022 March 31; published 2022 May 20

Abstract

We use IllustrisTNG simulations to explore the dynamic scaling relation between massive clusters and their—central—brightest cluster galaxies (BCGs). The IllustrisTNG-300 simulation we use includes 280 massive clusters from the $z = 0$ snapshot with $M_{200} > 10^{14}\ M_{\odot}$, enabling a robust statistical analysis. We derive the line-of-sight velocity dispersion of the stellar particles of the BCGs ($\sigma_{*,\mathrm{BCG}}$), analogous to the observed BCG stellar velocity dispersion. We also compute the subhalo velocity dispersion to measure the cluster velocity dispersion (σ_{cl}). Both $\sigma_{*,\mathrm{BCG}}$ and σ_{cl} are proportional to the cluster halo mass, but the slopes differ slightly. Thus, like the observed relation, $\sigma_{*,\mathrm{BCG}}/\sigma_{\mathrm{cl}}$ declines as a function of σ_{cl}, but the scatter is large. We explore the redshift evolution of the $\sigma_{*,\mathrm{BCG}} - \sigma_{\mathrm{cl}}$ scaling relation for $z \lesssim 1$ in a way that can be compared directly with observations. The scaling relation has a similar slope at high redshift, but the scatter increases because of the large scatter in $\sigma_{*,\mathrm{BCG}}$. The simulations imply that high-redshift BCGs are dynamically more complex than their low-redshift counterparts.

Unified Astronomy Thesaurus concepts: Brightest cluster galaxies (181); Galaxy clusters (584); Magnetohydrodynamical simulations (1966)

1. Introduction

Brightest cluster galaxies (BCGs) are a special population of luminous, massive galaxies. BCGs are usually found at the bottom of the cluster potential well indicated by the peak X-ray emission (e.g., Jones & Forman 1984; Postman & Lauer 1995; Lin & Mohr 2004; Sanderson et al. 2009; Lauer et al. 2014; Lopes et al. 2018). This coincidence indicates that the formation of BCGs is tightly associated with the formation of cluster halos.

Hierarchical structure formation models suggest that massive clusters form and evolve through stochastic accretion of surrounding material (e.g., van den Bosch 2002; McBride et al. 2009; Zhao et al. 2009; Fakhouri et al. 2010; Kravtsov & Borgani 2012; Haines et al. 2018). BCGs in the cluster grow through active accretion of other cluster members and material stripped from other galaxies. BCG evolution is more complex than cluster evolution because baryonic physics plays an important role.

Comparison between BCG and cluster mass tests the coevolution of a cluster and its BCG (e.g., Lin & Mohr 2004; Oliva-Altamirano et al. 2014; Lin et al. 2017; Kravtsov et al. 2018; Wen & Han 2018; Erfanianfar et al. 2019; Golden-Marx et al. 2022). Many studies derive the ratio between the stellar mass of a central galaxy and its host halo mass. The ratio between the stellar mass of a central galaxy and its host halo mass has a peak at $M_{\mathrm{halo}} \sim 10^{12}\ M_{\odot}$ (e.g., Conroy et al. 2006; Behroozi et al. 2010; Guo et al. 2010; Moster et al. 2010; Behroozi et al. 2019). In other words, the mass ratio declines as a function of halo mass within the cluster mass range. This decline suggests that the stellar mass growth of BCGs in massive halos is suppressed by strong feedback processes, including active galactic nuclei (e.g., Di Matteo et al. 2005; McNamara & Nulsen 2007; Kravtsov & Borgani 2012; Weinberger et al. 2017).

Sohn et al. (2020) explore the relation between BCGs and their host clusters based on dynamical properties measured from observations. They use the central stellar velocity dispersion ($\sigma_{*,\mathrm{BCG}}$) of the BCG, which probes the BCG subhalo mass. The central stellar velocity dispersion is proportional to the dark matter velocity dispersion, which is proportional to the dark matter halo mass (Zahid et al. 2018). Sohn et al. (2020) also compute the cluster velocity dispersion (σ_{cl}), which probes the cluster mass. These dynamical properties are powerful tools because they are insensitive to complex baryonic physics.

Sohn et al. (2020) show that $\sigma_{*,\mathrm{BCG}}/\sigma_{\mathrm{cl}}$ decreases as a function of σ_{cl}, based on the HeCS-omnibus sample, which compiles dense spectroscopy of 227 clusters. A similar relation appears in other cluster samples (e.g., Kim et al. 2017; Sohn et al. 2021). The decreasing $\sigma_{*,\mathrm{BCG}}/\sigma_{\mathrm{cl}}$ ratio at higher σ_{cl} indicates that the mass fraction associated with the BCG halo decreases in higher-mass clusters. Sohn et al. (2020) and Sohn et al. (2021) show that BCG growth in more massive clusters slows down, because the interactions between the BCG and other cluster members are suppressed by the large cluster velocity dispersion. BCGs in less massive clusters, where the cluster dispersion is comparable with the BCG central stellar velocity dispersion, can continue to grow.

Sohn et al. (2020) and Sohn et al. (2021) compare the observed $\sigma_{*,\mathrm{BCG}} - \sigma_{\mathrm{cl}}$ relation with theoretical relations from Dolag et al. (2010) and Remus et al. (2017). These theoretical relations predict that the $\sigma_{*,\mathrm{BCG}}/\sigma_{\mathrm{cl}}$ relation is constant over a large σ_{cl} range. Marini et al. (2021) revisit this issue using DIANOGA hydrodynamic zoom-in simulations. Marini et al. (2021) show that $\sigma_{*,\mathrm{BCG}}/\sigma_{\mathrm{cl}}$ declines slightly as a function of σ_{cl}; this revised theoretical relation is consistent with the observations.

Here we use the IllustrisTNG-300 cosmological hydrodynamic simulation (Springel et al. 2018) to investigate the $\sigma_{*,\mathrm{BCG}} - \sigma_{\mathrm{cl}}$ relation. Based on the 280 massive clusters from the $z = 0$ snapshot ($M_{200} > 10^{14}\ M_{\odot}$) in the IllustrisTNG simulation TNG300, we carry out a statistical exploration of clusters and

[4] Canada Research Chair in Astronomy and Astrophysics, Tier II.

their BCGs. For comparison with the observed data, we derive the $\sigma_{\rm cl}$ and $\sigma_{*,\rm BCG}$ from IllustrisTNG in analogy with the observed properties. We also investigate the redshift evolution of the $\sigma_{*,\rm BCG}-\sigma_{\rm cl}$ relation for $z\lesssim 1$, providing an important baseline for future cluster observations.

We describe the IllustrisTNG simulation and the techniques we use for deriving $\sigma_{*,\rm BCG}$ and $\sigma_{\rm cl}$ in Section 2. We demonstrate the simulated $\sigma_{BCG}-\sigma_{\rm cl}$ relation in Section 3.1. We compare the simulated and observed scaling relations in Section 3.2. We explore the redshift evolution of the scaling relations in Section 4. We conclude in Section 5. We adopt the Planck cosmological parameters (Planck Collaboration et al. 2016), with $H_0=67.74\,{\rm km\,s^{-1}\,Mpc^{-1}}$, $\Omega_m=0.3089$, and $\Omega_\Lambda=0.6911$.

2. Data

2.1. The IllustrisTNG Simulation

IllustrisTNG is a set of cosmological magnetohydrodynamic simulations of galaxy formation (Marinacci et al. 2018; Naiman et al. 2018; Nelson et al. 2018; Pillepich et al. 2018a; Springel et al. 2018). IllustrisTNG improves on its predecessor, Illustris (Vogelsberger et al. 2014a, 2014b), by extending the mass range of the simulated halos by simulating larger volumes. IllustrisTNG also includes an improved galaxy formation model that implements black hole–driven wind feedback, which affects the highest-mass galaxies (Weinberger et al. 2017; Pillepich et al. 2018a, 2018b).

We use the TNG300-1 simulation, selected from the set of IllustrisTNG simulations. TNG300 is one of the largest cosmological simulations, covering a ∼300 Mpc cube (Springel et al. 2018; Vogelsberger et al. 2020). The TNG300 set includes three simulations with different mass resolutions. We use TNG300-1 (hereafter, TNG300, for brevity), the highest-resolution simulation in this box size, with dark matter particle mass $m_{\rm DM}=59\times10^6\,M_\odot$ and target gas cell mass $m_{\rm baryon}=11\times10^6\,M_\odot$. The maximum physical softening length of stellar particles in TNG300 is set to 0.7 kpc.

The large volume of TNG300 enables the study of clusters and their BCGs based on a large number of simulated clusters. TNG300 includes 280 massive clusters with $M_{200}>10^{14}\,M_\odot$, five times larger than previous simulated cluster samples (e.g., Dolag et al. 2010; Bahé et al. 2017; Marini et al. 2021). The mass resolution of TNG300 is also better than in previous simulations (Vogelsberger et al. 2020). Our analysis extends and complements work by Marini et al. (2021), who explore the relation between the velocity dispersions of BCGs and their clusters with the DIAGONA set of simulations. These simulations provide a set of 57 simulated cluster halos with total dark matter mass larger than $7\times10^9\,M_\odot$, a much smaller sample than we obtain based on IllustrisTNG.

2.2. Cluster Velocity Dispersion

We use a group catalog derived from the TNG300 simulation to select cluster-like halos. TNG300 provides a group catalog that is constructed by applying a standard friends-of-friends algorithm with a fractional linking length $b=0.2$ times the mean separation of the galaxies at a given redshift. This group catalog lists the group properties, including the critical mass and size of the groups. Here, we obtain M_{200} (and R_{200}), the total mass of the group enclosed within a sphere of mean density 200 times the critical density at the group redshift (in this case, $z=0.0$).

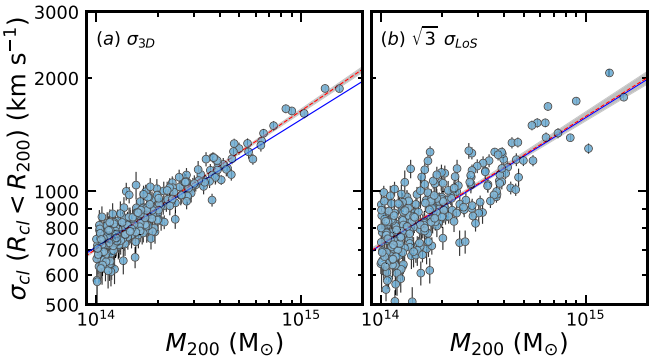

Figure 1. (a) The 3D velocity dispersion of cluster halos as a function of cluster mass (M_{200}). (b) The same as panel (a), but for the LOS velocity dispersion times $\sqrt{3}$. The gray shaded regions mark the 1σ distribution of the MCMC fits. The red lines show the best-fit power laws with slopes of $\alpha=0.368\pm0.008$ and 0.341 ± 0.016, respectively. The blue lines are the best-fit relation ($\alpha=0.339$) derived from Marini et al. (2021).

We select 280 massive group halos with $M_{200}>10^{14}\,M_\odot$ from the $z=0$ snapshot (hereafter, cluster halos). We apply this mass limit for comparison with observed clusters (see Section 2.4). This mass limit is comparable with the mass limits of other widely used cluster catalogs (e.g., the redMaPPer; Rykoff et al. 2014, 2016).

The group catalog also lists the properties of the subhalos belonging to each group halo. We use the position and velocity of the subhalos in the 280 massive cluster halos to compute the cluster velocity dispersion. We calculate the projected distance of the subhalos from the cluster halo center:

$$R_{\rm cl}=\sqrt{\Delta X^2+\Delta Y^2}, \quad (1)$$

where ΔX and ΔY are the separation between the subhalo and the central cluster halo positions, respectively.

We compute the velocity dispersion among the subhalos. This subhalo velocity dispersion corresponds to the observed cluster velocity dispersion. Observationally, the cluster velocity dispersion is the velocity dispersion of the cluster member galaxies (e.g., Sohn et al. 2020).

We also restrict the analysis to subhalos with stellar mass larger than $10^9\,M_\odot$, roughly corresponding to the stellar mass limit of dense spectroscopic surveys of massive clusters (Sohn et al. 2017). For direct comparison with the observed cluster velocity dispersion in Sohn et al. (2020), we derive the cluster velocity dispersion based on the subhalos within $R_{\rm cl}<R_{200}$. We then compute the cluster velocity dispersion based on 27 to 821 subhalos (with a median of 75). In analogy with the observed cluster velocity dispersion, we use the biweight technique (Beers et al. 1990) to compute the velocity dispersions. Hereafter, we refer to this measure as the cluster velocity dispersion ($\sigma_{\rm cl}$). We compute the cluster velocity dispersion uncertainty, the 1σ standard deviation, from 1000 bootstrap resamplings.

We note that our approach differs from previous works using numerical simulations (e.g., Dolag et al. 2010; Remus et al. 2017; Marini et al. 2021). Previous works measure the velocity dispersion of intracluster particles (Dolag et al. 2010; Remus et al. 2017) or the dark matter particles belonging to the cluster halo (Marini et al. 2021). Our approach of measuring the subhalo velocity dispersion provides a more direct comparison with the observed cluster velocity dispersion.

Because the simulation provides the three-dimensional (3D) distribution of the positions and velocities of subhalos, we can derive the 3D velocity dispersion. However, the 3D velocity

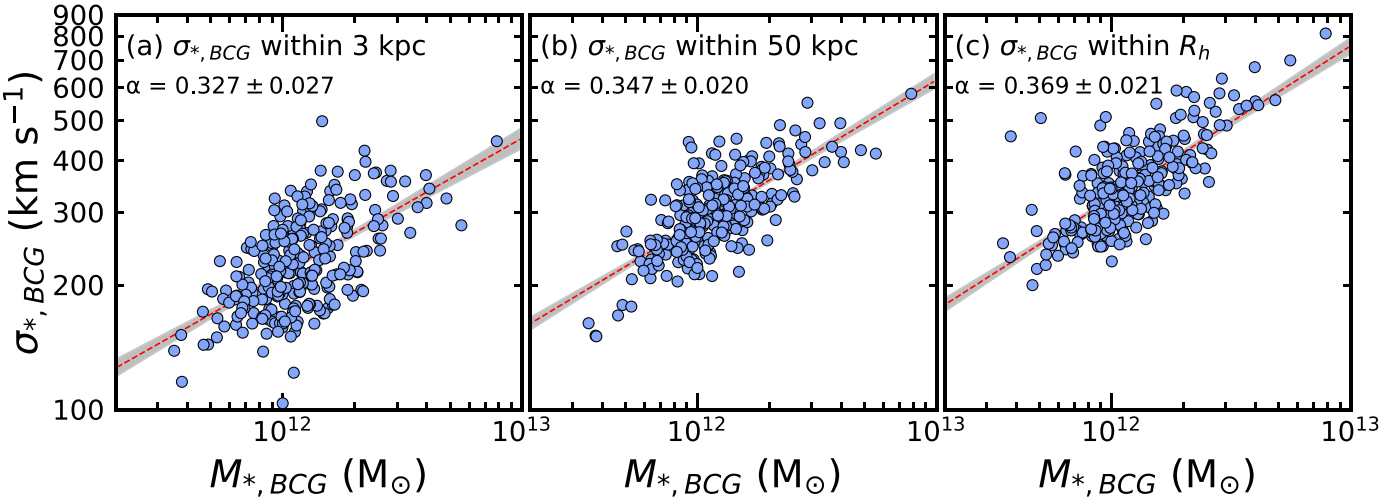

Figure 2. The LOS stellar velocity dispersion of the BCGs measured within (left) 3 kpc, (middle) 50 kpc, and (right) the half-mass radius as a function of the stellar mass of the BCGs. The red dashed lines show the best-fit relations. The gray shaded regions mark the 1σ distributions of the MCMC fits.

dispersion is not observable. Thus, we derive the observable line-of-sight (LOS) velocity dispersion of the subhalos based on the relative velocity differences between the subhalos and the cluster halo center in the $z-$direction.

Figure 1 shows the cluster velocity dispersion as a function of M_{200}. Figure 1(a) shows the 3D velocity dispersion and Figure 1(b) displays the LOS velocity dispersion (times $\sqrt{3}$). Both velocity dispersions are tightly correlated with M_{200}.

We derive the best-fit power-law relation $\sigma_{\rm cl} \propto M_{200}^{\alpha}$ following Marini et al. (2021). We use a Markov Chain Monte Carlo (MCMC) technique to derive the best-fit relations. The best-fit relation from the massive TNG halos has a slope $\alpha = 0.368 \pm 0.008$ for the 3D velocity dispersion and $\alpha = 0.343 \pm 0.016$ for the LOS velocity dispersion. These slopes are consistent with the slopes derived from other simulations (e.g., $\alpha = 0.339$; Marini et al. 2021). We also note that the 3D velocity dispersion is consistent with $\sigma_{\rm cl,LoS} \times \sqrt{3}$.

2.3. Velocity Dispersions of Brightest Cluster Galaxies

The group catalog from TNG300 lists the most massive subhalo in each group. We assume that the most massive subhalos correspond to the BCGs in the observations. Hereafter, we refer to the most massive subhalo in each of the 280 massive clusters as the BCG.

TNG300 provides the properties of the stellar particles that belong to each subhalo, which are identified by the SUBFIND algorithm. We select stellar particles within each of the 280 BCGs to compute the BCG velocity dispersion. We use the stellar particles within cylindrical volumes with three different apertures: (a) $R_{\rm proj} < 3$ kpc, (b) < 50 kpc, and (c) $< R_h$, where $R_{\rm proj} = \sqrt{\Delta X_*^2 + \Delta Y_*^2}$, and ΔX_* and ΔY_* are the distances between the stellar particles and the BCG subhalo center along the x-axis and y-axis, respectively. R_h is the comoving radius that contains half of the stellar mass of the subhalo. Thanks to the high resolution of TNG300, the BCGs in our sample include a large number of particles. For example, the BCG in the least massive cluster halo consists of 3855 stellar particles within a cylindrical volume with a 3 kpc projected radius. The number of stellar particles within this volume is large enough to apply the biweight technique to compute the velocity dispersion; Beers et al. (1990) suggest that the biweight technique performs well with samples larger than $n = 10$. Therefore, the BCG stellar velocity dispersion is insensitive to small-number statistics. In analogy with the observed BCG stellar velocity dispersion, we compute the LOS velocity dispersions of the stellar particles. We use the biweight technique to compute the BCG velocity dispersion. The BCG velocity dispersion uncertainty from 1000 bootstrap resamplings is tiny (<3 km s^{-1}).

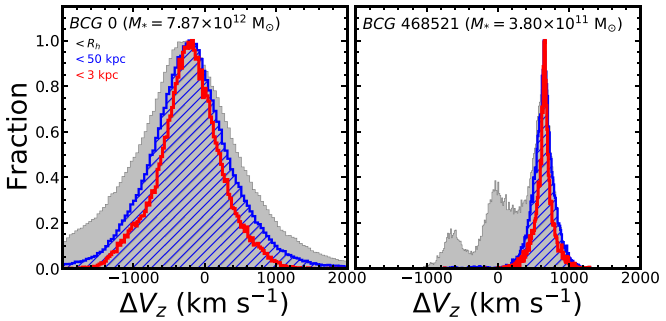

Figure 3. The LOS velocity distributions of the stellar particles within 3 kpc (the red open histogram), 50 kpc (the blue hatched histogram), and the half-mass radius (the gray filled histogram) in two BCG halos in our sample. The target BCGs are located in the most massive (left) and the least massive (right) clusters in our sample.

Figure 2 shows the stellar velocity dispersion of the BCGs as a function of the stellar mass of the BCGs. Here, the stellar mass of the BCGs is the total mass of all the stellar particles that are bound to the BCG subhalo (i.e., *SubhaloMassType*[4] in the TNG300 catalog).

The stellar velocity dispersion of the BCGs is correlated with the BCG subhalo mass. The red lines in Figure 2 show the best-fit power law ($\sigma_{*,\rm BCG} \propto M_{200}^{\alpha}$) based on the MCMC technique; the gray shaded regions show the 1σ distributions of the MCMC fits. The slopes of the relations vary from 0.327 to 0.369, depending on the aperture. Interestingly, the BCG velocity dispersion measured within a larger radius is generally more tightly correlated with the BCG mass.

The observed cluster sample is based on the BCG velocity dispersions measured within a fiducial 3 kpc aperture. Therefore, using the BCG subhalo velocity dispersion measured within 3 kpc enables direct comparison with the observations.

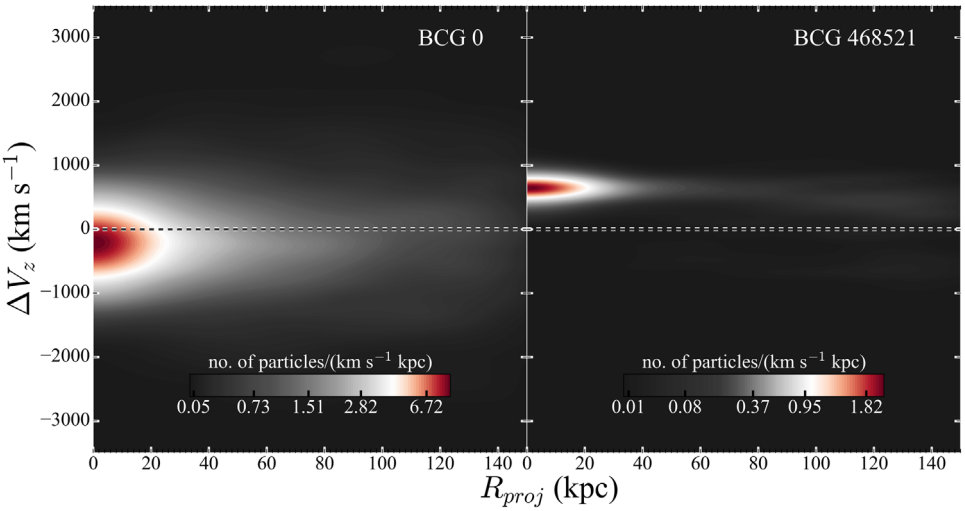

Figure 4. The LOS velocity as a function of projected distance (phase-space diagram) from the subhalo center of the stellar particles within the two BCG subhalos (the same BCGs as in Figure 3).

Figures 3 and 4 demonstrate another reason for using the velocity dispersion measured within a smaller aperture. For this demonstration, we select two BCGs in the most massive and the least massive cluster halos in our sample.

In Figure 3, we show the LOS velocity distributions of the stellar particles within 3 kpc (the red open histogram), 50 kpc (the blue hatched histogram), and R_h (the gray filled histogram) of the two BCGs. In Figure 4, we plot the phase-space diagram (often called the $R-v$ diagram) of the stellar particles of the BCGs; it shows the relative velocity difference of the stellar particles with respect to the BCG center as a function of projected distance from the BCG center.

In numerical simulations, separating the BCG subhalo from the entire cluster halo is not trivial. For example, Dolag et al. (2010) show that the stellar particles in the BCG subhalo in numerical simulations consist of two components (see also Marini et al. 2021); one population is governed by the entire cluster potential, and the other component is confined within the BCG subhalo. They derive the velocity dispersions of the two components, and interpret the small and large velocity dispersions that they derive as representing the BCG and the intracluster velocity dispersions, respectively.

In the most massive cluster, the stellar particles of the BCGs are extended in the LOS velocity direction at larger radius (the left panels of Figures 3 and 4). The stellar particles extended along the LOS may belong to the extended cluster halo, as suggested in Dolag et al. (2010; and also in Remus et al. 2017 and Marini et al. 2021). Using the velocity dispersion within a smaller aperture, where the density contrast is high, reduces contamination by the much lower density intracluster stellar component.

For the BCG in the less massive cluster (the right panels of Figures 3 and 4), the situation is more dramatic. In this BCG, the stellar particles associated with the BCG subhalo have multiple components; presumably this BCG is experiencing ongoing interactions. The disturbed stellar components appear at $R_{\rm proj} \gtrsim 30$ kpc, and they impact the velocity dispersion measurements. The velocity dispersion measured within 3 kpc is relatively insensitive to the ongoing activity. In other words, velocity dispersion measurement within 3 kpc is robust. We also note that the 3 kpc aperture is large enough compared to the maximum physical softening length of the stellar particles in TNG300. We measure the stellar velocity dispersion of the BCG subhalos within the 3 kpc aperture (see Section 2.3.). We therefore use the BCG velocity dispersion measured within 3 kpc (hereafter, $\sigma_{*,\rm BCG}$).

2.4. Comparison Sample from Observations

Our goal is to compare the $\sigma_{*,\rm BCG}-\sigma_{\rm cl}$ relation from TNG300 with the observed relation. For comparison, we use the HeCS-omnibus spectroscopic data compilation (Sohn et al. 2020) used to derive the observed $\sigma_{*,\rm BCG}-\sigma_{\rm cl}$ relation.

HeCS-omnibus includes 227 massive clusters with extensive spectroscopy. The spectroscopy comes from the Sloan Digital Sky Survey (SDSS) Data Release 16 (Ahumada et al. 2020), along with data collected from various MMT/Hectospec surveys, including CIRS (Rines & Diaferio 2006), HeCS (Rines et al. 2013), HeCS-SZ (Rines et al. 2016), HeCS-red (Rines et al. 2018), and ACReS (Haines et al. 2013). Based on large spectroscopic samples, Sohn et al. (2020) derive the physical properties of the clusters. First, they determine the spectroscopic membership of each cluster, based on the caustic technique (Diaferio & Geller 1997; Diaferio 1999; Serra & Diaferio 2013). The caustic technique yields an estimate of the characteristic cluster mass (i.e., M_{200}). Sohn et al. (2020) also compute the velocity dispersion for the cluster members within R_{200} using the biweight technique. This velocity dispersion corresponds to the subhalo velocity dispersion of the simulated cluster halos.

The HeCS-omnibus catalog also provides the physical properties of cluster members, including their stellar masses and central stellar velocity dispersions. Sohn et al. (2020) describe the details of these measurements. Here, we briefly introduce the stellar velocity dispersion measurements. For the majority (84/99) of the HeCS-omnibus BCGs, we obtain the stellar velocity dispersion from the Portsmouth reduction (Thomas et al. 2013), based on the Penalized Pixel-Fitting code (Cappellari & Emsellem 2004). There are 15 BCGs with MMT/Hectospec spectroscopy. For these BCGs, we use the University of Lyon Spectroscopic analysis Software (Koleva et al. 2009) to derive the velocity dispersion, by comparing the observed spectra with synthetic stellar population templates. Because of the large redshift range, the physical areas covered

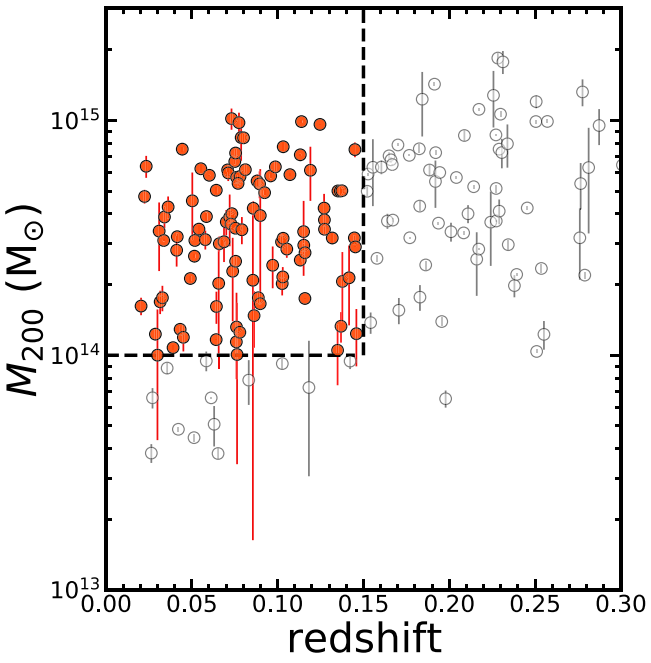

Figure 5. M_{200} of the HeCS-omnibus clusters (gray circles) as a function of redshift. The red filled circles show 99 clusters within $z < 0.15$ and $M_{200} > 10^{14}$ $M_\odot$ (the dashed lines), the comparison sample for TNG300.

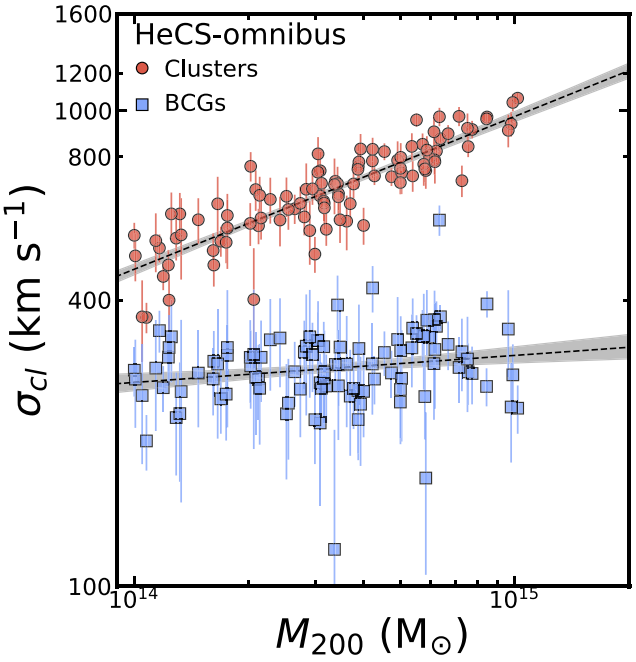

Figure 6. The LOS velocity dispersions of clusters (red circles) and their BCGs (blue squares) as a function of cluster mass (M_{200}) of the HeCS-omnibus clusters. The black dashed lines and gray shaded regions show the MCMC best-fit relations and their 1σ distributions.

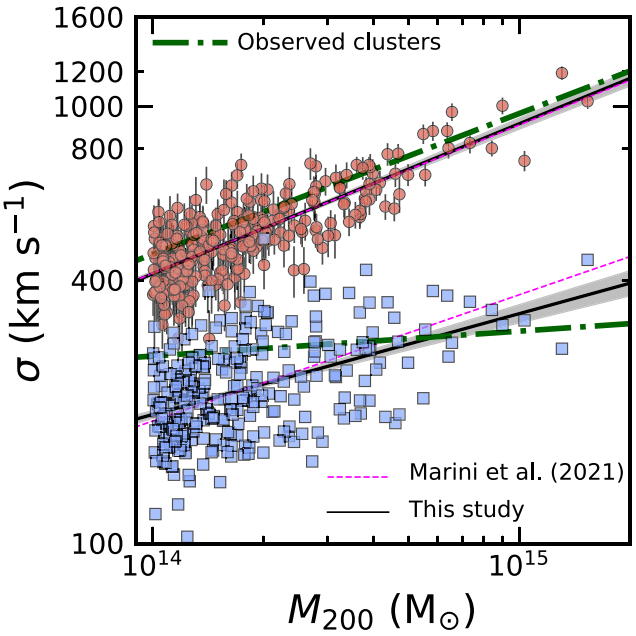

Figure 7. LOS velocity dispersions for clusters (red circles) and their BCGs (blue squares) as a function of cluster mass (M_{200}). The black lines show the best-fit relations. The gray shaded regions mark the 1σ distributions of the MCMC fits. The magenta lines show the best-fit relations from Marini et al. (2021). The green dotted–dashed lines show the observed $\sigma - M_{200}$ relations.

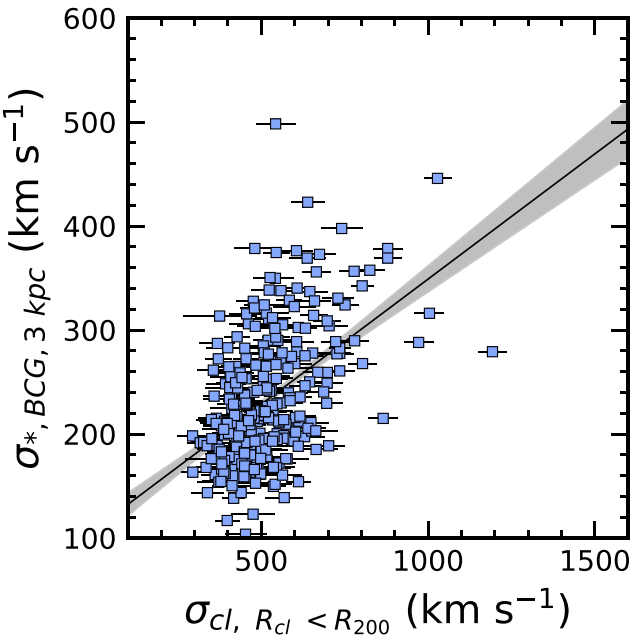

Figure 8. The BCG velocity dispersion as a function of cluster velocity dispersion. The solid line shows the best-fit relation. The gray shaded region shows the 1σ distribution of the MCMC fits.

by the SDSS/Hectospec fibers vary for the BCGs. We apply an aperture correction (see Zahid et al. 2016 and Sohn et al. 2017) to obtain the stellar velocity dispersion measured within a fiducial radius of 3 kpc. The aperture correction for the velocity dispersion is negligible (∼3%).

Figure 5 shows M_{200} of the HeCS-omnibus clusters as a function of cluster redshift. Most of the HeCS-omnibus clusters have masses larger than 10^{14} $M_\odot$, comparable with the mass limits of the other widely used cluster catalogs (e.g., the redMaPPer). We select HeCS-omnibus clusters with $M_{200} > 10^{14}$ $M_\odot$ for direct comparison with the halos in TNG300. We additionally apply a redshift selection ($z < 0.15$), because the HeCS-omnibus sample only includes a few most massive clusters at higher redshift. Furthermore, sampling clusters in a narrow redshift range is relatively insensitive to cluster evolution. The final comparison sample includes 99 HeCS-omnibus clusters with a median redshift of 0.08. We

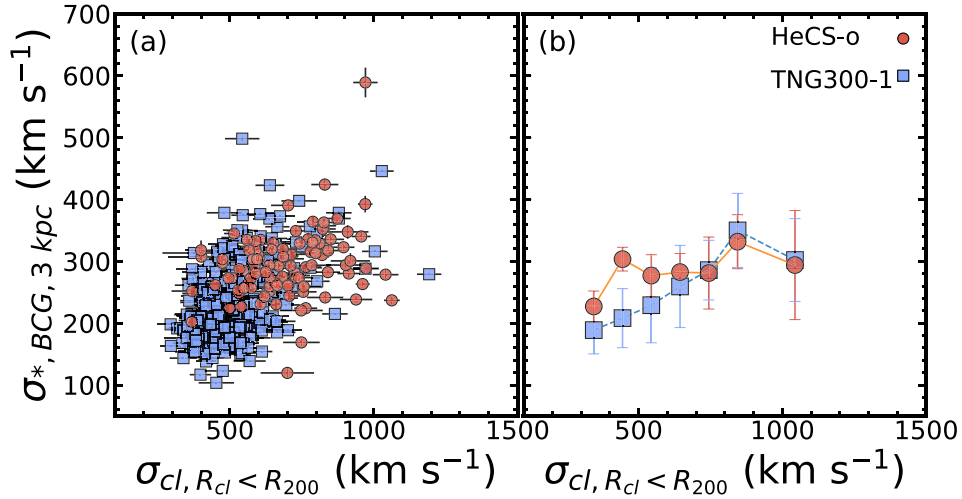

Figure 9. (a) $\sigma_{*,\mathrm{BCG,3kpc}}$ vs. σ_{cl} distributions of TNG clusters (blue squares) and HeCS-omnibus clusters (red circles). (b) The median distribution. The error bars indicates 1σ standard deviations.

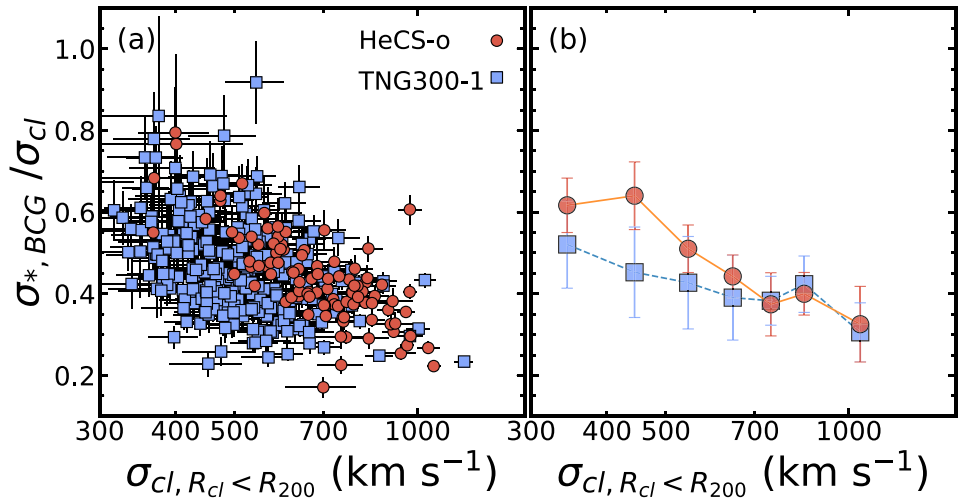

Figure 10. (a) The ratio between $\sigma_{*,\mathrm{BCG,\ 3\ kpc}}$ and σ_{cl} as a function of σ_{cl}. The x-axis is in log scale. (b) The median distribution of the $\sigma_{*,\mathrm{BCG,3kpc}}/\sigma_{\mathrm{cl}}$ ratio as a function of σ_{cl}.

compare this set of observed clusters with the simulated clusters at $z = 0.0$, assuming that evolution over this redshift range is negligible.

Figure 6 shows the $\sigma - M_{200}$ relation for the HeCS-omnibus clusters. The red circles and blue squares display the HeCS-omnibus clusters and their BCGs, respectively. The best-fit relations derived from the MCMC approach are:

$$\log \sigma_{\mathrm{cl}} = (0.322 \pm 0.019)\log M_{200} + (-1.846 \pm 0.178), \quad (2)$$

and

$$\log \sigma_{*,\mathrm{BCG}} = (0.057 \pm 0.031)\log M_{200} + (1.631 \pm 0.451), \quad (3)$$

respectively. We compare these relations with those derived from the simulated clusters in Section 3.

3. Results

Based on Illustris TNG300, we derive the physical properties of the simulated clusters and their BCGs. We use these properties to explore the correlation between the cluster and BCG properties. In Section 3.1, we explore various scaling relations for the clusters and BCGs. We compare the simulated relations with the data in Section 3.2.

3.1. Scaling Relations for TNG300 Clusters

Figure 7 displays the velocity dispersions of the clusters and their BCGs as a function of the mass of the cluster. Similar to Figure 1, we show the LOS velocity dispersions as a function of M_{200}. Both σ_{cl} and $\sigma_{*,\mathrm{BCG}}$ are correlated with M_{200}. We derive the best-fit relations:

$$\log \sigma_{\mathrm{cl},R_{\mathrm{cl}}<R_{200}} = (0.343 \pm 0.016)\log M_{200} + (-2.185 \pm 0.235), \quad (4)$$

and

$$\log \sigma_{*,\mathrm{BCG,3kpc}} = (0.230 \pm 0.027)\log M_{200} + (-0.930 \pm 0.384), \quad (5)$$

respectively. Interestingly, the $\sigma_{*,\mathrm{BCG}} - M_{200}$ relation is shallower than the $\sigma_{\mathrm{cl}} - M_{200}$ relation. This difference in slope

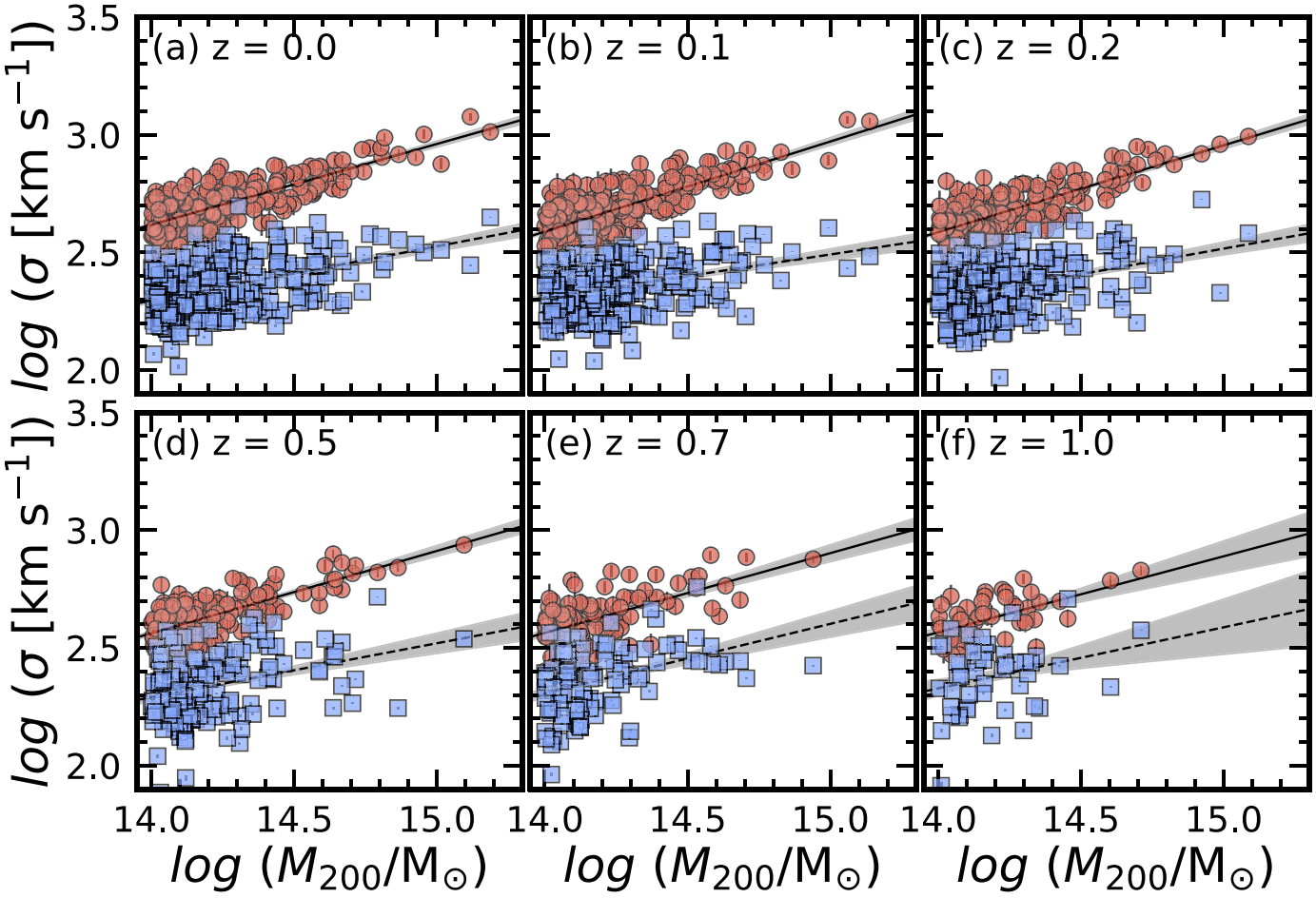

Figure 11. The same as Figure 7, but for six different redshift snapshots: (a) $z = 0.0$, (b) $z = 0.1$, (c) $z = 0.2$, (d) $z = 0.5$, (e) $z = 0.7$, and (f) $z = 1.0$. The solid and dashed lines show the best-fit relations. The gray shaded regions show the 1σ distributions of the MCMC fits.

is qualitatively consistent with the recent result of Marini et al. (2021). However, the slope of the $\sigma_{*,\mathrm{BCG}} - M_{200}$ relation in our sample is shallower than the relation (slope = 0.289) derived in Marini et al. (2021).

Figure 8 compares σ_{cl} and $\sigma_{*,\mathrm{BCG}}$. In general, higher-σ_{cl} clusters tend to host BCGs with large $\sigma_{*,\mathrm{BCG}}$, but the scatter is large at low σ_{cl}. The Spearman rank-order correlation test yields a correlation coefficient of 0.45 with a $p-$value of 1.56×10^{-15}. The Pearson correlation test yields a correlation coefficient of 0.49 with a $p-$value of 2.29×10^{-18}. We also derive the best-fit relation between σ_{cl} and $\sigma_{*,\mathrm{BCG}}$: $\sigma_{*,\mathrm{BCG}} = (0.295 \pm 0.049)\sigma_{\mathrm{cl}} + (95 \pm 25)$.

3.2. Comparison with HeCS-omnibus

We next compare the correlation between σ_{cl} and $\sigma_{*,\mathrm{BCG}}$ derived from the TNG300 halos at $z = 0$ with the observed relation. We describe the observational sample in Section 2.4.

We first compare the observed and simulated $\sigma - M_{200}$ relations. In Figure 7, the green dotted–dashed lines show the observed $\sigma - M_{200}$ relations. The relation for the cluster velocity dispersions is the same in both observations and simulations. In contrast, the observed $\sigma_{*,\mathrm{BCG}} - M_{200}$ relation is shallower than the simulated relation. In the simulated sample, there are many more BCGs with relatively low velocity dispersions ($\sigma_{*,\mathrm{BCG}} < 200\,\mathrm{km\,s^{-1}}$).

Figure 9(a) shows the $\sigma_{*,\mathrm{BCG}} - \sigma_{\mathrm{cl}}$ relation for the simulated clusters (blue squares) and for the observed HeCS-omnibus subsample (red circles; Section 2.4). The observed clusters overlap the simulated cluster sample. A difference between the two samples is the lack of observed clusters with small σ_{BCG}s at low σ_{cl} (i.e., $\sigma_{\mathrm{cl}} \lesssim 600\,\mathrm{km\,s^{-1}}$). Figure 9(b) demonstrates this difference; Figure 9(b) displays the median $\sigma_{*,\mathrm{BCG}}$ in various σ_{cl} bins. The median $\sigma_{*,\mathrm{BCG}}$ of the simulated clusters at $\sigma_{\mathrm{cl}} \lesssim 600\,\mathrm{km\,s^{-1}}$ is smaller than for the observed clusters; however, this difference is less than 2σ.

Figure 10(a) displays the ratio between $\sigma_{*,\mathrm{BCG}}/\sigma_{\mathrm{cl}}$ as a function of σ_{cl}. The observed clusters show a very tight relation: the ratio decreases as the cluster mass increases. Many simulated clusters overlap the observed clusters. However, there are more clusters with a low $\sigma_{*,\mathrm{BCG}}/\sigma_{\mathrm{cl}}$ ratio at $\sigma_{\mathrm{cl}} \lesssim 600\,\mathrm{km\,s^{-1}}$. These systems are absent in the observed sample. Figure 10(b) highlights this difference: the median ratio between the observed and simulated clusters differs slightly for $\sigma_{\mathrm{cl}} \lesssim 600\,\mathrm{km\,s^{-1}}$.

There are several interesting aspects of these comparisons. First, the trend that we derive from the TNG300 differs slightly from previous simulations. Dolag et al. (2010) and Remus et al. (2017) predict a constant ($\sigma_{*,\mathrm{BCG}}/\sigma_{\mathrm{cl}} \sim 0.5$) over a large σ_{cl} range. However, for a large fraction of the TNG300 clusters, $\sigma_{*,\mathrm{BCG}}/\sigma_{\mathrm{cl}}$ decreases as σ_{cl} increases. Furthermore, the median $\sigma_{*,\mathrm{BCG}}/\sigma_{\mathrm{cl}}$ is below the ratio predicted by the earlier simulations.

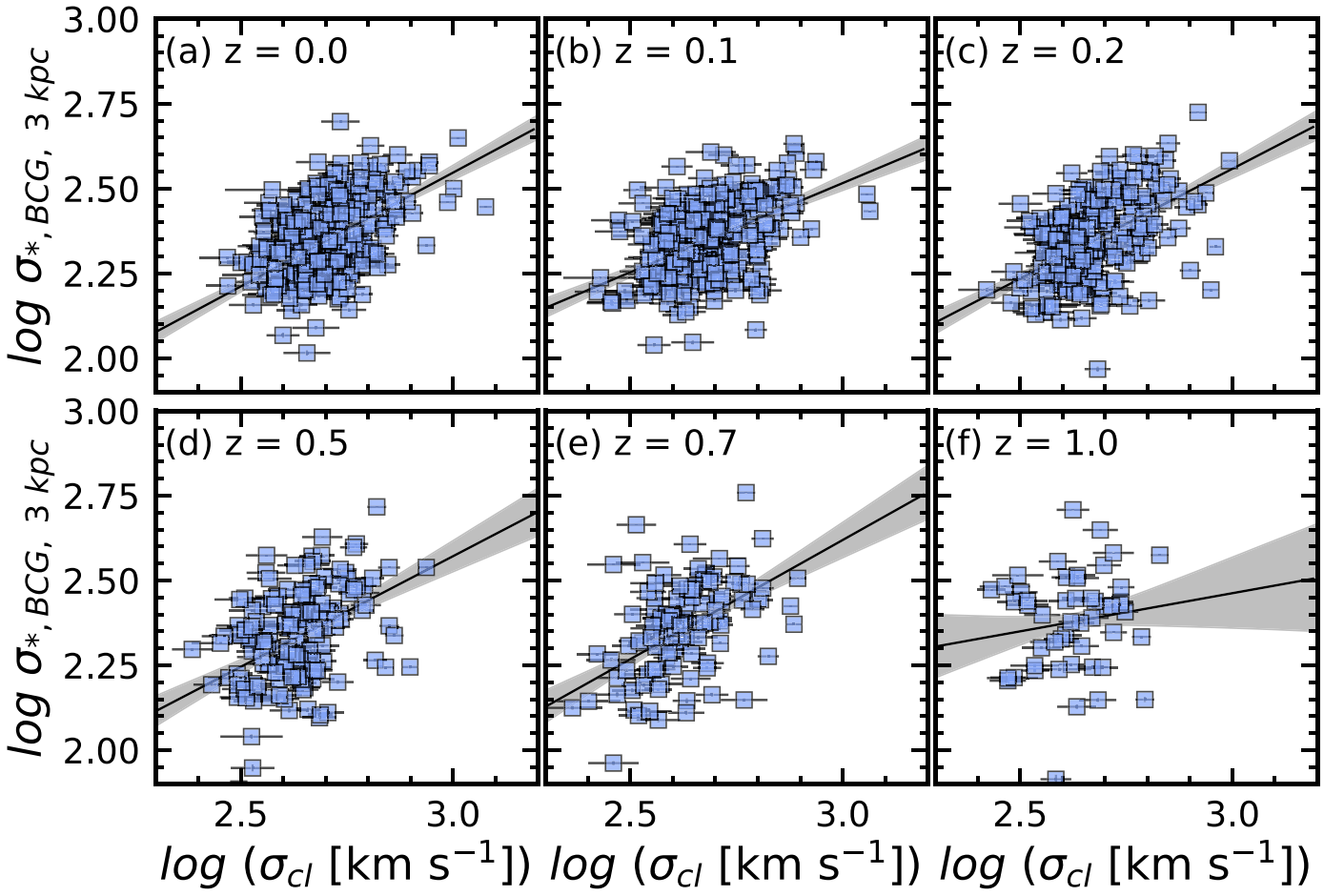

Figure 12. The same as Figure 8, but for the relation derived from six different redshift snapshots: (a) $z = 0.0$, (b) $z = 0.1$, (c) $z = 0.2$, (d) $z = 0.5$, (e) $z = 0.7$, and (f) $z = 1.0$. The gray shaded regions mark the 1σ distributions of the MCMC fits. The black solid lines show the best-fit relations.

Table 1
$\sigma_{*,\mathrm{BCG}} - \sigma_{\mathrm{cl}}$ Relation[a] at Different Redshifts

Redshift	α	β
0.0	0.67 ± 0.07	0.54 ± 0.20
0.1	0.53 ± 0.07	0.94 ± 0.19
0.2	0.65 ± 0.08	0.62 ± 0.22
0.5	0.65 ± 0.13	0.62 ± 0.33
0.7	0.70 ± 0.14	0.51 ± 0.36
1.0	0.23 ± 0.28	1.79 ± 0.72

Note.
[a] $\log \sigma_{*,\mathrm{BCG}} = \alpha \log \sigma_{\mathrm{cl}} + \beta$.

The result from TNG300 is consistent with more recent simulations. Marini et al. (2021) use the DIANOGA set of hydrodynamically simulated clusters to explore the $\sigma_{*,\mathrm{BCG}} - \sigma_{\mathrm{cl}}$ relation. In their simulation, Marini et al. (2021) show that the $\sigma_{*,\mathrm{BCG}}$ versus M_{200} relation is shallower than previously reported for the simulations of Dolag et al. (2010) and Remus et al. (2017). Consequently, the $\sigma_{*,\mathrm{BCG}} - \sigma_{\mathrm{cl}}$ relation derived by Marini et al. (2021) is consistent with the observed relation.

4. Redshift Evolution of the $\sigma_{*,\mathrm{BCG}} - \sigma_{\mathrm{cl}}$ Relation

Simulations like TNG300 enable the exploration of the evolution of the $\sigma_{*,\mathrm{BCG}} - \sigma_{\mathrm{cl}}$ relation at different redshifts. There are two approaches to exploring redshift evolution. First, we can trace the history of the most massive clusters and their BCGs identified in the current universe. For example, we select clusters and their BCGs in the current universe to derive the $\sigma_{*,\mathrm{BCG}} - \sigma_{\mathrm{cl}}$ relation. By measuring the properties of their progenitors at higher redshift, we can probe the redshift evolution of the correlation between the clusters and the BCGs. Marini et al. (2021) explore this relation for $0 < z < 2$. We plan to explore this evolution using TNG300 in a companion paper (J. Sohn et al. 2022, in preparation).

Here we take an approach more directly tied to observations to explore the redshift evolution of the $\sigma_{*,\mathrm{BCG}} - \sigma_{\mathrm{cl}}$ relation. We first select the most massive cluster halos at different redshifts. We then compare the cluster and BCG properties.

We select massive halos with $M_{200} > 10^{14}\ M_{\odot}$ at six different redshift snapshots (i.e., $z = 0.0$, 0.1, 0.2, 0.5, 0.7, and, 1.0). In each snapshot, there are 280, 250, 230, 149, 107, and 50 halos with $M_{200} > 10^{14}\ M_{\odot}$. We apply the same method that we used for the $z = 0$ sample to derive the velocity dispersions of clusters and their BCGs.

Figure 11 shows σ_{cl} (red circles) and $\sigma_{*,\mathrm{BCG}}$ (blue squares) as a function of cluster mass (M_{200}) at six different redshifts. σ_{cl} is tightly correlated with M_{200} over the redshift range. However, the correlation between $\sigma_{*,\mathrm{BCG}}$ and M_{200} is less tight at higher redshift.

We plot the $\sigma_{*,\mathrm{BCG}} - \sigma_{\mathrm{cl}}$ relation at six different redshifts (Figure 12). The solid lines show the best-fit linear relations based on the MCMC technique. Table 1 summarizes the slopes

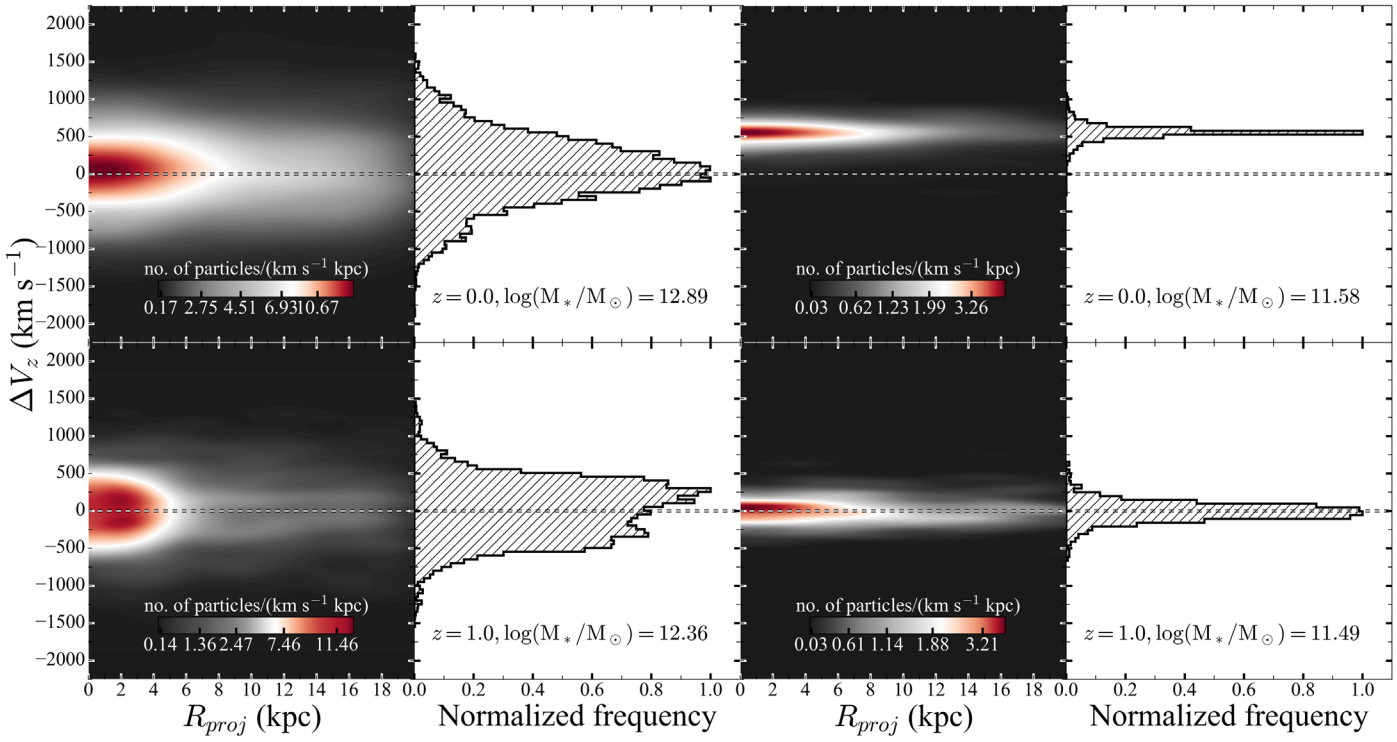

Figure 13. $R - v$ diagrams (left) and LOS velocity distributions (right) of the stellar particles within BCGs at $z = 0$ (top panels) and $z = 1$ (bottom panels). The BCGs at each redshift lie within the most massive (left two panels) and least massive (right two panels) clusters.

of these best-fit relations; the slopes and their uncertainties correspond to the median and 1σ standard deviations of the MCMC fits.

There are two notable changes in the relation as a function of redshift. First, the range of $\sigma_{\rm cl}$ broadens as the universe ages. The $\sigma_{\rm cl}$ of $M_{200} > 10^{14}\ M_\odot$ clusters at $z = 1$ ranges from 270 to 674 km s^{-1}; at $z = 0$, the range is 294–1192 km s^{-1}. The maximum $\sigma_{\rm cl}$ increases by $\sim$70%.

Second, in contrast to the $\sigma_{\rm cl}$ ranges, the range of $\sigma_{*,\rm BCG}$ narrows at lower redshifts: $82 < \sigma_{*,\rm BCG}\,({\rm km\,s^{-1}}) < 510$ at $z = 1.0$ to $103 < \sigma_{*,\rm BCG}\,({\rm km\,s^{-1}}) < 498$ at $z = 0.0$. Additionally, the $\sigma_{*,\rm BCG}$ of a cluster with a similar $\sigma_{\rm cl}$ at higher redshift is generally larger than for its counterpart at lower redshift. As a consequence, the slope of the $\sigma_{*,\rm BCG} - \sigma_{\rm cl}$ relation changes, although the uncertainty is large.

A decreasing $\sigma_{*,\rm BCG}$ over time appears inconsistent with the general idea that the mass of a BCG subhalo ($\propto\sigma_{*,\rm BCG}$) grows via accretion and mergers as the universe ages. However, the $\sigma_{*,\rm BCG}$ measurement is sensitive to the dynamical stages of the BCGs, particularly when the BCGs undergo active interactions with other galaxies (Figure 4). The interactions between BCGs and other cluster members occur more frequently at higher redshift, where BCGs are actively forming.

Figure 13 demonstrates the dynamically unrelaxed nature of the BCGs at higher redshift. The upper panels of Figure 13 display the $R - v$ diagrams of the stellar particles within two BCGs at $z = 0$. These BCGs are the most massive subhalos in the most massive (left) and least massive (right) clusters. We also show the LOS velocity distributions of the stellar particles within $R_{\rm proj} < 1$ kpc in the panels adjacent to the $R - v$ diagrams. The lower panels show similar BCGs at $z = 1$.

The difference between the $R - v$ diagrams of the most massive BCGs at $z = 0$ and $z = 1$ (left panels) is dramatic. The BCG at $z = 0$ shows well-defined trumpet-like patterns in the core and an extended distribution in the outer region ($R_{\rm proj} > 5$ kpc). In contrast, the most massive BCG at $z = 1$ shows a complex structure in the core ($R_{\rm proj} < 1$ kpc; LOS velocity distribution). This structure presumably inflates the velocity dispersion. Less massive BCGs at $z = 1$ also show elongated stellar distributions along the LOS. These elongations exceed those of BCGs with similar mass at $z = 0.0$. Furthermore, the high-redshift BCGs show more clumpy structures in the outer region.

The redshift evolution of the $\sigma_{*,\rm BCG} - \sigma_{\rm cl}$ relation offers a unique test bed for observational studies of cluster and BCG formation. The next-generation spectroscopic surveys, including DESI, 4MOST, and the Subaru Prime Focus Spectrograph, will increase the spectroscopic samples of clusters at $z < 1$. A large number of clusters at high redshift with velocity dispersion measurements based on large numbers of members will then be available. The central stellar velocity dispersions of the BCGs in these high-redshift clusters will also be measured.

5. Conclusion

We explore the $\sigma_{*,\rm BCG} - \sigma_{\rm cl}$ scaling relation based on IllustrisTNG simulations. TNG300 includes 280 massive clusters with $M_{200} > 10^{14}\ M_\odot$. We measure the LOS velocity dispersion of the stellar particles within 3 kpc of the BCG center as $\sigma_{*,\rm BCG}$. We compute the LOS velocity dispersion of the cluster members within $R_{\rm cl} < R_{200}$ as $\sigma_{\rm cl}$. These $\sigma_{\rm cl}$ and $\sigma_{*,\rm BCG}$ correspond to the properties of observed clusters.

Both $\sigma_{*,\rm BCG}$ and $\sigma_{\rm cl}$ of the simulated clusters are correlated with the halo mass (M_{200}). The $\sigma_{*,\rm BCG} - M_{200}$ scaling relation shows a larger scatter than the $\sigma_{\rm cl} - M_{200}$ scaling relation. The slopes of the relation differ: the $\sigma_{*,\rm BCG} - M_{200}$ relation is slightly shallower than the $\sigma_{\rm cl} - M_{200}$ relation. This difference

in slope produces a $\sigma_{*,\mathrm{BCG}} - \sigma_{\mathrm{cl}}$ relation with a slope that departs from unity.

We compare the $\sigma_{*,\mathrm{BCG}} - \sigma_{\mathrm{cl}}$ scaling relation with that derived from the HeCS-omnibus sample. Overall, the simulated and observed scaling relations overlap. In the simulation, there are many clusters with low σ_{cl} (<600 km s^{-1}) and low $\sigma_{*,\mathrm{BCG}}$ (<200 km s^{-1}). These systems are absent in HeCS-omnibus. The lack of these systems presumably results from selection effects in HeCS-omnibus; less massive clusters with less massive BCGs are excluded at least in part as a result of the selection of X-ray luminosity. The low-σ_{cl} clusters make the simulated scaling relation slightly steeper than the observed relation, but the difference is within the uncertainty.

We trace the $\sigma_{*,\mathrm{BCG}} - \sigma_{\mathrm{cl}}$ scaling relations as a function of redshift. We select massive cluster halos with $M_{200} > 10^{14}\ M_{\odot}$ at six different redshifts $\lesssim 1$. We sample the simulations in a way that provides a direct test bed for future high-redshift observations of these scaling relations.

$\sigma_{*,\mathrm{BCG}}$ is correlated with σ_{cl} over the redshift range ($z < 1.0$) we explore. However, the correlation is weaker for massive clusters at higher redshift because of the large scatter in $\sigma_{*,\mathrm{BCG}}$. The BCGs in the higher-redshift massive cluster are actively interacting with other cluster members, inflating the velocity dispersion. Future observations of high-redshift clusters and their BCGs will provide a clean test for these models.

We thank the anonymous referee for insightful comments. We thank Josh Borrow for carefully reading the draft and for providing valuable comments that improved the paper. We also thank Antonaldo Diaferio and Ken Rines for helpful discussions. J.S. is supported by the CfA Fellowship. M.J.G. acknowledges the Smithsonian Institution for support. M.V. acknowledges support through NASA ATP 19-ATP19-0019, 19-ATP19-0020, and 19-ATP19-0167, and NSF grants AST-1814053, AST-1814259, AST-1909831, AST-2007355, and AST-2107724. M.V. also acknowledges support from an MIT RSC award, the Alfred P. Sloan Foundation, and NASA ATP grant NNX17AG29G. I.D. acknowledges the support of the Canada Research Chair Program and the Natural Sciences and Engineering Research Council of Canada (NSERC, funding reference No. RGPIN-2018-05425).

All of the primary TNG simulations have been run on the Cray XC40 Hazel Hen supercomputer at the High Performance Computing Center Stuttgart (HLRS) in Germany. They have been made possible by the Gauss Centre for Supercomputing (GCS) large-scale project proposals GCS-ILLU and GCS-DWAR. GCS is the alliance of the three national supercomputing centers HLRS (Universitaet Stuttgart), JSC (Forschungszentrum Julich), and LRZ (Bayerische Akademie der Wissenschaften), funded by the German Federal Ministry of Education and Research (BMBF) and the German State Ministries for Research of Baden-Wuerttemberg (MWK), Bayern (StMWFK), and Nordrhein-Westfalen (MIWF). Further simulations were run on the Hydra and Draco supercomputers at the Max Planck Computing and Data Facility (MPCDF, formerly known as RZG) in Garching near Munich, in addition to the Magny system at HITS in Heidelberg. Additional computations were carried out on the Odyssey2 system supported by the FAS Division of Science, Research Computing Group at Harvard University, and the Stampede supercomputer at the Texas Advanced Computing Center through the XSEDE project AST140063.

ORCID iDs

Jubee Sohn https://orcid.org/0000-0002-9254-144X
Margaret J. Geller https://orcid.org/0000-0002-9146-4876
Mark Vogelsberger https://orcid.org/0000-0001-8593-7692
Ivana Damjanov https://orcid.org/0000-0003-4797-5246

References

Ahumada, R., Prieto, C. A., Almeida, A., et al. 2020, ApJS, 249, 3
Bahé, Y. M., Barnes, D. J., Dalla Vecchia, C., et al. 2017, MNRAS, 470, 4186
Beers, T. C., Flynn, K., & Gebhardt, K. 1990, AJ, 100, 32
Behroozi, P., Wechsler, R. H., Hearin, A. P., & Conroy, C. 2019, MNRAS, 488, 3143
Behroozi, P. S., Conroy, C., & Wechsler, R. H. 2010, ApJ, 717, 379
Cappellari, M., & Emsellem, E. 2004, PASP, 116, 138
Conroy, C., Wechsler, R. H., & Kravtsov, A. V. 2006, ApJ, 647, 201
Di Matteo, T., Springel, V., & Hernquist, L. 2005, Natur, 433, 604
Diaferio, A. 1999, MNRAS, 309, 610
Diaferio, A., & Geller, M. J. 1997, ApJ, 481, 633
Dolag, K., Murante, G., & Borgani, S. 2010, MNRAS, 405, 1544
Erfanianfar, G., Finoguenov, A., Furnell, K., et al. 2019, A&A, 631, A175
Fakhouri, O., Ma, C.-P., & Boylan-Kolchin, M. 2010, MNRAS, 406, 2267
Golden-Marx, J. B., Miller, C. J., Zhang, Y., et al. 2022, ApJ, 928, 28
Guo, Q., White, S., Li, C., & Boylan-Kolchin, M. 2010, MNRAS, 404, 1111
Haines, C. P., Pereira, M. J., Smith, G. P., et al. 2013, ApJ, 775, 126
Haines, C. P., Finoguenov, A., Smith, G. P., et al. 2018, MNRAS, 477, 4931
Jones, C., & Forman, W. 1984, ApJ, 276, 38
Kim, J.-W., Ko, J., Hwang, H. S., et al. 2017, ApJ, 836, 105
Koleva, M., Prugniel, P., Bouchard, A., & Wu, Y. 2009, A&A, 501, 1269
Kravtsov, A. V., & Borgani, S. 2012, ARA&A, 50, 353
Kravtsov, A. V., Vikhlinin, A. A., & Meshcheryakov, A. V. 2018, AstL, 44, 8
Lauer, T. R., Postman, M., Strauss, M. A., Graves, G. J., & Chisari, N. E. 2014, ApJ, 797, 82
Lin, Y.-T., Hsieh, B.-C., Lin, S.-C., et al. 2017, ApJ, 851, 139
Lin, Y.-T., & Mohr, J. J. 2004, ApJ, 617, 879
Lopes, P. A. A., Trevisan, M., Laganá, T. F., et al. 2018, MNRAS, 478, 5473
Marinacci, F., Vogelsberger, M., Pakmor, R., et al. 2018, MNRAS, 480, 5113
Marini, I., Borgani, S., Saro, A., et al. 2021, MNRAS, 507, 5780
McBride, J., Fakhouri, O., & Ma, C.-P. 2009, MNRAS, 398, 1858
McNamara, B. R., & Nulsen, P. E. J. 2007, ARA&A, 45, 117
Moster, B. P., Somerville, R. S., Maulbetsch, C., et al. 2010, ApJ, 710, 903
Naiman, J. P., Pillepich, A., Springel, V., et al. 2018, MNRAS, 477, 1206
Nelson, D., Pillepich, A., Springel, V., et al. 2018, MNRAS, 475, 624
Oliva-Altamirano, P., Brough, S., Lidman, C., et al. 2014, MNRAS, 440, 762
Pillepich, A., Nelson, D., Hernquist, L., et al. 2018a, MNRAS, 475, 648
Pillepich, A., Springel, V., Nelson, D., et al. 2018b, MNRAS, 473, 4077
Planck Collaboration, Ade, P. A. R., Aghanim, N., et al. 2016, A&A, 594, A13
Postman, M., & Lauer, T. R. 1995, ApJ, 440, 28
Remus, R.-S., Dolag, K., & Hoffmann, T. 2017, Galax, 5, 49
Rines, K., & Diaferio, A. 2006, AJ, 132, 1275
Rines, K., Geller, M. J., Diaferio, A., & Kurtz, M. J. 2013, ApJ, 767, 15
Rines, K. J., Geller, M. J., Diaferio, A., & Hwang, H. S. 2016, ApJ, 819, 63
Rines, K. J., Geller, M. J., Diaferio, A., Hwang, H. S., & Sohn, J. 2018, ApJ, 862, 172
Rykoff, E. S., Rozo, E., Busha, M. T., et al. 2014, ApJ, 785, 104
Rykoff, E. S., Rozo, E., Hollowood, D., et al. 2016, ApJS, 224, 1
Sanderson, A. J. R., Edge, A. C., & Smith, G. P. 2009, MNRAS, 398, 1698
Serra, A. L., & Diaferio, A. 2013, ApJ, 768, 116
Sohn, J., Geller, M. J., Diaferio, A., & Rines, K. J. 2020, ApJ, 891, 129
Sohn, J., Geller, M. J., Hwang, H. S., et al. 2021, ApJ, 923, 143
Sohn, J., Geller, M. J., Zahid, H. J., et al. 2017, ApJS, 229, 20
Springel, V., Pakmor, R., Pillepich, A., et al. 2018, MNRAS, 475, 676
Thomas, D., Steele, O., Maraston, C., et al. 2013, MNRAS, 431, 1383
van den Bosch, F. C. 2002, MNRAS, 331, 98
Vogelsberger, M., Genel, S., Springel, V., et al. 2014a, Natur, 509, 177
Vogelsberger, M., Genel, S., Springel, V., et al. 2014b, MNRAS, 444, 1518
Vogelsberger, M., Marinacci, F., Torrey, P., & Puchwein, E. 2020, NatRP, 2, 42
Weinberger, R., Springel, V., Hernquist, L., et al. 2017, MNRAS, 465, 3291
Wen, Z. L., & Han, J. L. 2018, MNRAS, 481, 4158
Zahid, H. J., Geller, M. J., Fabricant, D. G., & Hwang, H. S. 2016, ApJ, 832, 203
Zahid, H. J., Sohn, J., & Geller, M. J. 2018, ApJ, 859, 96
Zhao, D. H., Jing, Y. P., Mo, H. J., & Börner, G. 2009, ApJ, 707, 354